10-1-2015

First-principles calculations of the lattice thermal conductivity of the lower mantle

Stephen Stackhouse
University of Leeds

Lars Stixrude
University College London

Bijaya B. Karki
Louisiana State University

Recommended Citation

Stackhouse, S., Stixrude, L., & Karki, B. (2015). First-principles calculations of the lattice thermal conductivity of the lower mantle. *Earth and Planetary Science Letters, 427*, 11-17. https://doi.org/10.1016/j.epsl.2015.06.050

First-principles calculations of the lattice thermal conductivity of the lower mantle

Stephen Stackhouse[a,*], Lars Stixrude[b], Bijaya, B. Karki[c]

[a] *School of Earth and Environment, University of Leeds, Leeds LS2 9JT, United Kingdom.*

[b] *Department of Earth Sciences, University College London, Gower Street, London WC1E 6BT, United Kingdom.*

[c] *School of Electrical Engineering and Computer Science, Department of Geology and Geophysics, and Center for Computation and Technology, Louisiana State University, Baton Rouge, LA70803, United States of America.*

**E-mail addresses: s.stackhouse@leeds.ac.uk; l.stixrude@ucl.ac.uk; karki@csc.lsu.edu*

Abstract

The temperature variations on top of the core-mantle boundary are governed by the thermal conductivity of the minerals that comprise the overlying mantle. Estimates of the thermal conductivity of the most abundant phase, $MgSiO_3$ perovskite, at core-mantle boundary conditions vary by a factor of ten. We performed ab initio simulations to determine the lattice thermal conductivity of $MgSiO_3$ perovskite, finding a value of 6.8 ± 0.9 W m^{-1} K^{-1} at core-mantle boundary conditions (136 GPa and 4000 K), consistent with geophysical constraints for the thermal state at the base of the mantle. Thermal conductivity depends strongly on pressure, explaining the dynamical stability of super-plumes. The dependence on temperature and composition is weak in the deep mantle: our results exhibit saturation as the phonon mean free path approaches the interatomic spacing. Combining our results with seismic tomography, we find large lateral variations in the heat-flux from the core that have important implications for core dynamics.

Keywords

$MgSiO_3$ perovskite; thermal conductivity; mantle dynamics

1. Introduction

Heat-flux at the core-mantle boundary has important implications for the thermal evolution of the core and mantle (Lay et al., 2008), the size and stability of plumes (Dubuffet et al., 1999), and generation of the magnetic field (Gubbins et al., 2011). Despite this, there is a wide range of estimates of the thermal conductivity of the lower mantle (Osako and Ito, 1991; Hofmeister, 2008; Goncharov et al., 2010; de Koker, 2010; Manthilake et al., 2011; Haigis et al., 2012; Ohta et al., 2012; Dekura et al., 2013; Tang et al., 2014; Ammann et al., 2014; Ohta et al., 2014). As insulators and semi-conductors, the major lower mantle phases: (Mg,Fe)SiO_3 perovskite, $CaSiO_3$ perovskite, and (Mg,Fe)O ferropericlase are expected to conduct heat via phonons (lattice vibrations), but experimental and theoretical studies of their lattice thermal conductivity have suffered significant limitations.

Technical constraints mean that experimental measurements are limited to temperature much lower than those in the deep Earth, and thus long extrapolations must be made to estimate values in the lowermost mantle. In addition, while the results of ambient temperature studies of $MgSiO_3$ perovskite (Osako and Ito, 1991; Ohta et al., 2012) are in reasonable agreement, measurements at elevated temperature (500-1100 K) and 26 GPa (Manthilake et al., 2011), suggests a 300 K lattice thermal conductivity almost twice as large. This suggests that there are discrepancies even at low temperature and pressure.

Classical simulations, where simple functional forms define interactions between atoms, also have considerable uncertainties. Haigis et al. (2012) used a classical potential to compute lattice thermal conductivity via equilibrium molecular dynamics and Green-Kubo relations, while Ammann et al. (2014) used a classical potential to calculate lattice thermal conductivity via non-equilibrium molecular dynamics simulations. The difference of up to a factor of two between the studies, for the lattice thermal conductivity of $MgSiO_3$ perovskite, illustrates the uncertainty due to the choice of classical potential. This source of

uncertainty has been highlighted in other studies (Chen et al., 2012; Howell, 2012) and shows the importance of performing ab initio calculations, where forces are calculated from first-principles.

Previous ab initio calculations of the lattice thermal conductivity of $MgSiO_3$ perovskite have also suffered important limitations. Dekura et al. (2013) and Tang et al. (2014) performed lattice dynamics calculations, which are limited by the assumption that anharmonic terms are truncated at third-order. The truncation is significant, because it requires the lattice thermal conductivity to vary as the inverse of the temperature (T^{-1}), more rapidly than observed in silicates and oxide perovskites at temperatures greater than the Debye temperature (Marquardt et al., 2009a; Hofmeister, 2010), and leads to underestimation of the conductivity at high temperature.

Here, we take a different approach, calculating the lattice thermal conductivity of $MgSiO_3$ perovskite using the 'direct' non-equilibrium molecular dynamics method (NEMD), with forces calculated directly from density functional theory. The direct method, which we have used previously to compute the lattice thermal conductivity of MgO periclase (Stackhouse et al., 2010), has the advantage that anharmonicity is fully included with no truncation. The method is conceptually straightforward: lattice thermal conductivity is calculated from Fourier's law by computing the temperature gradient induced by an imposed heat-flux.

2. Theory

2.1 Non-Equilibrium Molecular Dynamics Simulations

The lattice thermal conductivity of $MgSiO_3$ perovskite was calculated using ab initio non-equilibrium molecular dynamics (Stackhouse and Stixrude, 2010). The method is intuitive, following the design of experimental techniques. The simulation cell is divided up into sections (Fig. 1(a)). One section is designated the 'hot section' and another the 'cold section'. These are separated by a distance of half the length of the simulation cell. At

regular intervals heat is transferred from the cold section to the hot section, generating a heat-flux. Over time, a temperature gradient develops between the hot and cold sections (Fig. 1(b)). Once steady state is reached thermal conductivity is calculated from Fourier's law:

$$k = - \frac{\langle J(t) \rangle}{\langle dT / dx \rangle} \quad (1)$$

where k is the thermal conductivity, and $\langle J(t) \rangle$ and $\langle dT/dx \rangle$ are the time average of the heat-flux and the temperature gradient.

In order to conserve the total kinetic energy and linear momentum of the system, the transfer of energy from the cold section to the hot section is achieved by assigning the hottest atom in the cold section and coldest atom in the hot section the velocities that would arise from a hypothetical elastic collision between them (Müller-Plathe, 1997; Nieto-Draghi and Avalos, 2003).

The temperature gradient is determined from a linear fit to the temperature of the individual sections. Due to the periodic nature of the simulation, heat enters and leaves from both sides of the hot and cold sections and two temperature gradients develop, leading to a temperature profile resembling that shown in Fig. 1(b). Rather than discard one of them, the temperature of symmetrically equivalent sections is averaged. Due to the non-Newtonian nature of the energy transfer, the temperature gradient is non-linear around the hot and cold sections. In view of this, these sections are excluded from the fit to determine the temperature gradient (Supplementary Material Fig. S1(d)).

2.2 Finite-Size Effects

Our analysis of finite-size effects follows that of Schelling et al. (2002) and has been used widely as a means of obtaining results in the limit of infinite systems (Zhou et al., 2009;

Sellan et al., 2010; Howell, 2011a, 2011b, 2012; Hu et al., 2011). Kinetic theory relates thermal conductivity to phonon mean free path

$$k = \frac{1}{3} C_v v l \tag{2}$$

where C_v is the volumetric heat capacity, v is the mean sound velocity and l is the phonon mean free path. Since phonons are scattered within the hot and cold sections, the longest possible phonon mean free path is equal to the distance between them, i.e. half the length of the simulation cell. If the true phonon mean free path is much longer than this, the thermal conductivity calculated will be significantly underestimated.

If we assume that the phonon mean free path is dependent on two independent scattering mechanisms: phonon-phonon scattering and phonon-boundary scattering occurring at the hot and cold sections, then the effective mean free path for a simulation cell of length L is

$$l_L^{-1} = l_{ph}^{-1} + l_b^{-1} \tag{3}$$

where l_{ph} is the contribution from phonon-phonon scattering and l_b the contribution from phonon-boundary scattering. l_b is assumed to be $L/4$, where L is the total length of the simulation cell. The factor of 4 arises because phonons originating between the hot and cold sections will travel, on average, a quarter of the simulation cell length before encountering the hot and cold sections. Substituting Eq. (3) into (2) and rearranging leads to

$$k_L^{-1} = k_\infty^{-1} + bL^{-1} \tag{4}$$

where k_L is the thermal conductivity calculated for a simulation cell of length L, k_∞ the thermal conductivity of a simulation cell of infinite length (i.e. the true value) and b a constant equal to

$$b = \frac{12}{C_v v} \quad (5)$$

Thus by calculating the thermal conductivity for simulation cells of different length and plotting against L^{-1}, one can estimate $k_{¥}^{-1}$.

Previous studies (Sellan et al., 2010; Howell, 2012) have shown that the linear extrapolation (Eq. (4)) may be inaccurate when the phonon mean free path is much longer than the smallest simulation cell. For example, studies of silicon near room temperature, which has a long phonon mean free path, require simulation cells on the order of 10 000 atoms. In the case of our calculations, smaller simulations cells are sufficient, since the temperature is much higher and the phonon mean free path much shorter (Tadano et al., 2014). In our previous calculations of periclase (Stackhouse et al., 2010), we used simulation cells of a similar size, and found our results to be in good agreement with other theoretical methods and experimental results, and the phonon mean free path to be shorter than the smallest simulation cell.

Phonon mean free paths can be estimated from the slope of the linear relationship between k_L^{-1} and L^{-1}, combining Eqs. (2) and (5)

$$l = \frac{bk_{¥}}{4} \quad (6)$$

Estimated values of l (Supplementary Material Table S1) are shorter than the shortest simulation cell used at all temperature and pressures studied, indicating that our simulation cells are large enough to obtain accurate results.

Calculations may also be inaccurate if the cross-sectional area of the simulation cell is too small (Schelling et al., 2002; Zhou et al., 2009; Hu et al., 2011). This is because the phonon population is then biased towards those propagating in the long direction of the simulation cell, leading to an overestimate of the thermal conductivity. This is not expected

to be a serious issue in our simulations, because the phonon mean free path is comparable to the cross-sectional dimensions. To test this issue, we have performed simulations with different cross-sectional areas at 110 GPa and 1000 K and 110 GPa and 3250 K. The results are identical within uncertainty (Supplementary Material Table S1).

3 Calculation Details

Calculations were performed using a version of the density functional theory based VASP code (Kresse and Furthmuller, 1996a, 1996b) modified to perform NEMD. The local density approximation (Perdew and Zunger, 1981) was used for the exchange-correlation functional. Ultrasoft pseudopotentials were employed, with valence electron configurations: $3s^2$ for Mg, $3s^2 3p^2$ for Si and $2s^2 2p^4$ for O. The kinetic-energy cut-off for the plane-wave basis set was set to 400 eV and Brillouin zone sampling was restricted to the Γ-point. Fermi-smearing was applied in all calculations, with a broadening-width equal to the simulation temperature. The convergence criteria for the self-consistency loop was 10^{-4} eV. The time-step was set to 1 fs and the Nosé thermostat was employed to maintain a constant temperature (Nosé, 1984). By calculating the forces from first-principles, we avoid issues associated with empirical pair potentials (Chen et al., 2012; Howell, 2012).

The dimensions of all simulation cells used in the current work are listed in Supplementary Material Table S2. The cell parameters at each pressure and temperature (P-T) point, were determined from equilibrium molecular dynamics simulations using 80 atom $MgSiO_3$ models.

Before each NEMD calculation, the simulation cell was equilibrated by performing 1 ps of equilibrium molecular dynamics, after which energy exchange was initiated. The energy exchange periods used are listed in Supplementary Materials Table S2. These were chosen to produce a temperature difference of 500-1000 K between the hot and cold sections and took values of between 40-80 fs. Simulations using longer exchange periods

converged more slowly, and led to values with larger associated uncertainties, because the error in the temperature gradient increased. Initial tests showed that, within a certain range, using different exchange periods had little effect on the results (Supplementary Materials Fig. S2).

Most NEMD calculations were run for a minimum of about 50 ps (Supplementary Material Table S2), at least 10 ps of which was allowed for steady state to be reached. Thermal conductivity was calculated using the remaining portion. In general, this led to converged values for the heat-flux, temperature gradient and thermal conductivity (Supplementary Material Fig. S1). When a simulation was judged not to have converged fully i.e. the time average of the thermal conductivity had not have flattened out, simulations were run longer.

The uncertainty in the time average of the heat-flux was determined using the appropriate statistics (Flyvbjerg and Petersen, 1989), taking into account correlation. The same method was also used to compute the uncertainty in the time average of the temperature of individual sections. To calculate the temperature gradient the temperatures of symmetrically equivalent sections were averaged and fit using weighted least square regression, but excluding the values for the hot and cold sections and those either side of them (Fig. S1(d)). The thermal conductivity for a simulation cell of infinite length was determined from a weighted least squares fit to a plot of inverse thermal conductivity against inverse simulation cell length (Supplementary Material Figs. S3 and S4). The extrapolated values are listed in Supplementary Material Table S1.

4. Results

At lower mantle conditions, we find that the temperature dependence of the thermal conductivity is weak: at 75 GPa, lattice thermal conductivity decreases from 5.3 ± 0.7 $Wm^{-1}K^{-1}$ at 2500 K to 4.7 ± 0.8 at 4000 K (Fig. 2). Note that, our results indicate that the lattice

thermal conductivity of $MgSiO_3$ perovskite is isotropic at 75 GPa and 2500 K to within the uncertainty of our results (Fig. S3 and Table S1), and this is presumed to be the case at all other conditions. All values shown in Figs. 2 and 3 are for the [100] direction. Both here and throughout the manuscript the uncertainties indicate the standard error. This variation is weaker than the often-assumed T^{-1} dependence, and even weaker than the $T^{-2/5}$ dependence recently suggested for $MgSiO_3$ perovskite, based on experimental results at lower pressures and temperatures (Manthilake et al., 2011). Such weak temperature dependence indicates saturation (Roufosse and Klemens, 1974; Marquardt et al., 2009a; Hofmeister, 2010), where the phonon mean free path approaches the inter-atomic spacing. This means that pressure (or density) dependence dominates throughout most of the lower mantle: at 4000 K, lattice thermal conductivity increases from 5.3 ± 0.7 $Wm^{-1}K^{-1}$ at 75 GPa to 9 ± 2 $Wm^{-1}K^{-1}$ at 145 GPa (Fig. 2).

Our results agree well with room temperature experimental data (Osako and Ito, 1991; Ohta et al., 2012; Ohta et al. 2014), showing comparable pressure dependence. The measurements of Manthilake et al. (2011), show similar temperature dependence, but are higher by about 5 $Wm^{-1}K^{-1}$ (Fig. 2 (main)). We note that their results also disagree with the ambient temperature values of Ohta et al. (2012). Lattice dynamics calculations of Dekura et al. (2013) agree with our results at low temperature, as expected, but predict a value half that of our study at core-mantle boundary conditions. We attribute this difference to the truncation of anharmonic terms at third order in the lattice dynamics calculation, which assumes T^{-1} behavior and does not capture the saturation (Roufosse and Klemens, 1974) that we find at high temperature. The values of Tang et al. (2014), which also suffer from truncation of anharmonic terms, are much lower than all other studies. It has been proposed that finite-size effects in NEMD simulations lead to erroneous values (Haigis et al., 2012), but this issue is expected to be minimal for $MgSiO_3$ perovskite at lower mantle conditions, where the phonon mean free path is short and lattice thermal conductivity is

low (Supplementary Material Fig. S4 and Table S1) (Tadano et al., 2014). Indeed, previous simulations based on classical potentials and much larger systems show remarkably similar values of the thermal conductivity at the core-mantle boundary (Ammann et al., 2014).

5. Discussion

Our results serve as a test of approximate theories of the density and temperature dependence of the thermal conductivity. Our results disagree with the commonly assumed T^{-1} or $T^{-1/2}$ temperature dependence. Instead, we find that our results are reproduced well by a model (Supplementary Material Section S1) that combines the Leibfried-Schlömann equation with temperature dependence that includes the effects of saturation (Roufosse and Klemens, 1974)

$$k \propto \frac{M\overline{\Omega}^{1/3}\gamma^3}{\gamma^2 T}\left\{\frac{2}{3}\left[\frac{T_S(\overline{\Omega})}{T}\right]^{1/2}+\frac{1}{3}\left[\frac{T}{T_S(\overline{\Omega})}\right]\right\}C \qquad (7)$$

where M is the mean atomic mass, Ω mean atomic volume, θ Debye temperature, γ Grüneisen parameter, T temperature, and $T_S \mu M\Omega^{2/3}\theta^2/\gamma^2$ is the temperature at which saturation becomes significant. The term in the brackets accounts for saturation and causes k to vary more weakly than $T^{-1/2}$ at high temperature, in excellent agreement with our results. The heat capacity C, accounts for phonon population effects at low temperature. All quantities are computed from a thermodynamic model (Stixrude and Lithgow-Bertelloni, 2011). The two constants of proportionality are chosen by fitting to our NEMD results.

We estimate the lattice thermal conductivity across the lower mantle, arriving at a value of 8.1 ± 1.1 $Wm^{-1}K^{-1}$ at the core-mantle boundary (Fig. 3), by combining the results of the present work, with our earlier ab initio predictions for periclase (Stackhouse et al., 2010),

and scaling laws for minor phases and impurities (Supplementary Material Sections S2 to S4). We approximate the lower mantle as pyrolite: (Mg,Fe)SiO_3 perovskite (75 percent), $CaSiO_3$ perovskite (6 percent) and (Mg,Fe)O ferropericlase (19 percent) (Stixrude and Lithgow-Bertelloni, 2011). Recent experimental results show that iron impurities greatly reduce lattice thermal conductivity (Manthilake et al., 2011), at least at the low temperatures at which the measurements were made. By assuming this same large reduction, previous studies (Manthilake et al., 2011; Haigis et al., 2012) arrived at values for the lattice thermal conductivity of the lower mantle similar to ours. However, we expect the impact of impurities to be reduced at lower mantle temperatures. Based on the theory of Klemens (1960), we estimate the fractional lowering of the lattice thermal conductivity of the lower mantle due to iron impurities to be 8 percent at the core-mantle boundary, i.e. our value at the core-mantle boundary in the iron-free limit is very similar: 8.8 ± 1.2 $Wm^{-1}K^{-1}$. The influence of aluminum is expected to be less than that of iron (Ohta et al., 2014). Our value for an iron-free lower mantle is substantially smaller than that estimated in a recent experimental study (Manthilake et al., 2011) which we attribute to the long extrapolation from the experimental results to lower mantle conditions. Our value is a factor of 2 larger than the estimate based on the lattice dynamics calculations of Dekura et al. (2013) and a factor of 6 larger than that based on the lattice dynamics calculations of Tang et al. (2014), which we attribute to the truncation of anharmonic terms in these studies.

The thermal conductivity of iron-bearing phases may be influenced by electronic transitions at lower mantle conditions. The influence of the high-spin to low-spin transition on thermal conductivity is unknown. If we assume that the primary effect of the transition is to decrease the atomic spacing, and take the volume decrease of Tsuchiya et al. (2006), based on scaling relations (Supplementary Material Section S2), the lattice thermal conductivity of ferropericlase may be 3 percent higher in the low-spin state than in the

high-spin state. Within the transition region, in which high-spin and low-spin iron coexists in variable amounts, the mean acoustic wave velocity is reduced. If we assume that bulk sound velocity is reduced by the amount reported by Wentzcovitch et al. (2009) and that the shear velocities are unaffected (Marquardt et al., 2009b), based on scaling relations (Supplementary Material Section S2), the lattice thermal conductivity may be 15 percent smaller than the high-spin phase. The influence of the spin transition of the lattice thermal conductivity of perovskite will be much less than in ferropericlase, because of the lower iron content and the smaller fraction of ferrous iron. The spin transition appears to decrease photon thermal conductivity and reduce the electrical conductivity (Goncharov et al., 2010). Although pure FeO becomes metallic at high pressures and temperatures (Fischer et al., 2011), thermal transport by electrons is unlikely to contribute significantly to thermal conductivity for plausible mantle iron concentrations. Extreme enrichment in iron, i.e. Fe/Si ~ 1, may produce much greater thermal conductivity by stabilizing new phases in which heat transport by electrons becomes important (Manga and Jeanloz, 1996), but seismic evidence rules out such extreme enrichments, even in ultra-low velocity zones (Rost et al., 2005).

In addition to scattering from impurities, scattering from interactions with electrons and grain boundaries can also influence lattice thermal conductivity. In the lower mantle, $(Mg,Fe)SiO_3$ perovskite, $CaSiO_3$ perovskite and (Mg,Fe)O ferropericlase are insulators and semiconductors. Older studies of semiconductors (e.g. Boghosian and Dubey, 1978) suggest that phonon-electron scattering is only important at low temperature (< 5 K), but a more recent first-principles investigation (Liao et al., 2015) shows that, for silicon with high carrier concentrations ($> 10^{19}$ cm^{-3}), it has a marked effect at room temperature. There are no studies of the effect of phonon-electron scattering at lower mantle conditions, but we note that the analysis of Liao et al. (2015) indicates that phonon-electron scattering is most significant for phonons with a mean free path greater than 100 nm. This is much longer

than that expected for phonons in $MgSiO_3$ perovskite (Supplementary Material Table S1) and MgO periclase (Stackhouse et al. 2010), at lower mantle conditions. Inclusion of impurities will reduce the phonon mean free paths of the phases further. In view of this, we conclude that the effect of phonon-electron scattering is negligible in the lower mantle.

The effect of phonon-boundary scattering on lattice thermal conductivity becomes important when the mean free path is comparable to the grain size. Imada et al. (2014) showed that, at 300 K, there is a significant difference between single- and poly-crystal lattice thermal conductivity measurements for MgO periclase, in particular, at high pressure where the phonon mean free path is long in the single-crystal. Their analysis suggests that at core-mantle boundary conditions the lattice thermal conductivity of the phase will be independent of grain size, because of the much shorter mean free path. Since the mean free path of phonons in $MgSiO_3$ perovskite and iron-bearing phases is expected to be even shorter than that of MgO periclase, the lattice thermal conductivity of the lower mantle should be independent of grain size.

In some regions of the lower few hundred kilometers of the mantle, it is expected that perovskite transforms to post-perovskite (Wookey et al., 2005). Some studies indicate that the lattice thermal conductivity of post-perovskite is a factor of two greater than that of perovskite (Ohta et al., 2012; Ammann et al., 2014), but others suggest that this is only true at the low temperatures at which the experiments were conducted and at high temperature the difference is much smaller (Haigis et al., 2012). In view of this, we ignore differences in the lattice thermal conductivities of the two phases. We also neglect possible radiative contributions to the thermal conductivity, because measurements show that these are less than 0.5 $Wm^{-1}K^{-1}$ (Goncharov et al., 2008). However, we note that a consensus has not yet been reached: another experimental study concludes that the radiative contribution could be up to 5 $Wm^{-1}K^{-1}$ (Keppler et al., 2008).

Our predicted value of the thermal conductivity at the core-mantle boundary is consistent with a variety of geophysical constraints (Lay et al., 2008). A boundary layer analysis (Supplementary Material Section S4) shows that for a thermal boundary layer thickness δ ~ 100 km (Fig. 4), our results satisfy independent constraints on the temperature across the thermal boundary layer from extrapolation of the mantle geotherm and inner-core freezing; the location of the seismic discontinuities caused by the perovskite to post-perovskite phase transition; and bounds on the heat-flow from intra-plate volcanism and heat conducted down the core adiabat.

The increase in thermal conductivity with increasing depth (Fig. 3) that we find – nearly a factor of two across the lower mantle – is dynamically significant. Greater thermal conductivity at depth is essential for stabilizing so-called superplumes: large-scale structures in the bottom-most 1000 km of the mantle beneath Africa and the Pacific, with very low shear wave velocity indicating higher than average temperature (Dziewonski et al., 2010). Dynamical simulations (Dubuffet et al., 1999) show that the buoyant instability of hot superplumes can be counter-acted and their long-term stability explained if the thermal conductivity of the lower mantle is higher than the rest of the mantle, just as we find.

While the physical model outlined in the previous sections completely specifies the calculation of the lattice thermal conductivity at all pressure and temperature conditions, we recognize that it may be useful to have a simpler, approximate form that captures the essence of these results. We present a simple approximation to the variation of the lattice thermal conductivity of pyrolite with pressure and temperature that is value across the lower mantle regime

$$k = (4.9\ \mathrm{GPa} + 0.105P) f \left(\frac{T}{1200K}\right)\left(\frac{1200K}{T}\right) \qquad (8)$$

where k is thermal conductivity ($Wm^{-1}K^{-1}$), P is pressure (GPa), T is temperature (K) and f is a function based on the theory of Roufosse and Klemens (1974), which accounts for saturation (Supplementary Material Section S1). This equation reproduces our results for pyrolite to within 10 percent along mantle geotherms with potential temperatures between 1000 K and 2000 K and with or without a bottom thermal boundary layer and over the entire lower mantle pressure regime.

According to our results the thermal conductivity in the lower mantle is nearly homogeneous laterally, because of the weak dependence that we find on temperature and impurities. For example, varying the temperature by ± 500 K, changes the thermal conductivity at the core-mantle boundary by only 5 percent. Superplumes may also be stabilized by chemical heterogeneity; indeed seismic evidence of sharp sides indicates that they have a different chemical composition from normal mantle (Ni et al., 2002). We find that, in the lower mantle, the influence of chemical heterogeneity on thermal conductivity is minor (e.g. doubling the Fe/Mg ratio decreases the conductivity by only 5 percent). This idea was also suggested by Manthilake et al. (2011), who showed that iron concentration has little effect on the lattice thermal conductivity of (Mg,Fe)O ferropericlase, although we note that they estimate a much larger difference between an iron-free and iron-bearing lower mantle (50 percent) than that found in this study (8 percent). It was suggested by Ohta et al. (2012), that the difference between iron-free and iron-bearing phases observed in lower pressure measurements (< 26 GPa) by Manthilake et al. (2011) should be diminished at lower mantle pressures where iron will exist in a low-spin state. Enrichment in aluminum is expected to have a smaller effect, because of the similarity in atomic mass of aluminum to magnesium and silicon. This is assumption is supported by the results of Ohta et al. (2014), but conflicts with those of Manthilake et al. (2011).

Lateral homogeneity in thermal conductivity at the core-mantle boundary is significant, because it implies a direct relationship between the temperature in the lower-most mantle, which can be inferred from seismology (Kustowski et al., 2008), and lateral variations in the heat-flux across the core-mantle boundary, via Fourier's law (Nakagawa and Tackley, 2008). Combining Fourier's law for the heat-flux $q = k\partial T/\partial z$, with a linear temperature profile near the core-mantle boundary $T = T_{CMB} - h\partial T/\partial z$, and scaling of shear-wave velocity to temperature $\xi = (\partial \ln V_S/\partial T)_z$ we find lateral variations in the heat-flux $dq = -k/h \, d\ln Vs/\xi$, where T is temperature, z is depth, T_{CMB} is the temperature at the core-mantle boundary, h is height above the core-mantle boundary, and V_S is shear-wave velocity. To compute dq we use our value of k for pyrolite at the core-mantle boundary, $d\ln V_S$ from seismic tomography at 2800 km depth, giving h = 90 km, and the scaling ξ from a thermodynamic model (Stixrude and Lithgow-Bertelloni, 2011). We do not include the influence of the perovskite to post-perovskite transition on ξ because the pressure at which the transition occurs is uncertain. We find substantial lateral variation in heat-flux, comparable in magnitude to the mean value (Fig. 5). The heat-flux varies from zero (i.e. no heat escaping the core) to nearly twice the mean value. Such large later variations in heat-flux have important implications for our understanding of the origin of Earth's magnetic field (Olson and Christensen, 2002), its behaviour during reversals (Glatzmaier et al., 1999), and the structure of the inner core (Gubbins et al., 2011). Geodynamo simulations (Gubbins et al., 2011) indicate that even for much smaller lateral variation in heat flow than we estimate, localized melting of the inner core may occur, which may help to explain anomalies in the structure of the inner core including its radial structure, anisotropy, and hemispherical dichotomy. We note that our estimates of the lateral variation of heat flux are based on the assumption that lateral variations in seismic wave velocity are purely thermal in origin. An

395 understanding of the contributions of lateral variations in chemistry to the tomographic
396 signal will be important for understanding the pattern of heat flow.

397 **6. Conclusions**

398 In conclusion, our calculations suggest that the lattice thermal conductivity of $MgSiO_3$
399 perovskite depends strongly on pressure, but that temperature and compositional
400 dependence is weak in the deep mantle. Combining our results with seismic tomography,
401 we find large lateral variations in the heat-flux from the core that have important
402 implications for core dynamics. Our predictions of the thermal conductivity provide a firm
403 basis from which further to explore the influence of mantle chemical heterogeneity on the
404 coupled thermal evolution of core and mantle.

405

406

Acknowledgements

This research was supported by the European Research Council under Advanced Grant No. 291432 “MoltenEarth” (FP7/2007-2013), NERC grant number NE/K006290/1 and the National Science Foundation through TeraGrid resources provided by the Texas Advanced Computing Center, under NSF grant EAR080017. In addition, we also acknowledge the use of high performance computing provided by Advanced Research Computing at the University of Leeds and HECToR, the UK's national high-performance computing service, which is provided by UoE HPCx Ltd at the University of Edinburgh, Cray Inc and NAG Ltd, and funded by the Office of Science and Technology through EPSRC's High End Computing Programme. The authors thank Carolina Lithgow-Bertelloni for assistance preparing Fig. 5, and the editor and two anonymous reviewers for constructive comments. S.S. thanks Michael Ammann, John Brodholt, David Dobson, and Andrew Walker for useful discussions.

References

Ammann, M.W., Walker, A.M., Stackhouse, S., Wookey, J., Forte, A.M., Brodholt, J.P., Dobson, D.P., 2014. Variation of thermal conductivity and heat flux at the Earth's core mantle boundary. Earth Planet. Sci. Lett. 390, 175–185.

Boghosian, H.H., Dubey, K.S., 1978. Role of Electron-Phonon Interaction and Peripheral Phonons in the Lattice Thermal Conductivity of Doped Semiconductor at Low Temperatures. Phys. Stat. Sol. 88, 417-427.

Chen, Y., Chernatynskiy, A., Brown, D., Schelling, P.K., Artacho, E., Phillpot, S.R., 2012. Critical assessment of classical potentials for MgSiO3 perovskite with application to thermal conductivity. Phys. Earth Planet. Inter. 210-211, 75–89.

Davies, G.F., 2007. Mantle regulation of core cooling: A geodynamo without core radioactivity? Phys. Earth Planet. Inter. 160, 215–229.

de Koker, N., 2010. Thermal conductivity of MgO periclase at high pressure: Implications for the D'' region. Earth Planet. Sci. Lett. 292, 392–398.

Dekura, H., Tsuchiya, T., Tsuchiya, J., 2013. Ab initio Lattice Thermal Conductivity of MgSiO3 Perovskite as Found in Earth's Lower Mantle. Phys. Rev. Lett. 110, 025904.

Dubuffet, F., Yuen, D.A., Rabinowicz, M., 1999. Effects of a realistic mantle thermal conductivity on the patterns of 3-D convection. Earth Planet. Sci. Lett. 171, 401–409.

Dziewonski, A.M., Lekic, V., Romanowicz, B.A., 2010. Mantle Anchor Structure: An argument for bottom up tectonics. Earth Planet. Sci. Lett. 299, 69–79.

Fischer, R.A., Campbell, A.J., Lord, O.T., Shofner, G.A., Dera, P., Prakapenka, V.B., 2011. Phase transition and metallization of FeO at high pressures and temperatures. Geophys. Res. Lett. 38, L24301.

453 Flyvbjerg, H., Petersen, H., 1989. Error-estimates on averages of correlated data. J.
454 Chem. Phys. 91, 461–466.
455 Glatzmaier, G.A., Coe, R.S., Hongre, L., Roberts, P.H., 1999. The role of the Earth's
456 mantle in controlling the frequency of geomagnetic reversals. Nature 401, 885–890.
457 Goncharov, A.F., Haugen, B.D., Struzhkin, V.V., Beck, P., Jacobsen, S.D., 2008.
458 Radiative conductivity in the Earth's lower mantle. Nature 456, 231–234.
459 Goncharov, A.F., Struzhkin, V.V., Montoya, J.A., Kharlamova, S., Kundargi, R., Siebert, J.,
460 Badro, J., Antonangeli, D., Ryerson, F.J., Mao, W., 2010. Effect of composition,
461 structure, and spin state on the thermal conductivity of the Earth's lower mantle.
462 Phys. Earth Planet. Inter. 180, 148–153.
463 Gubbins, D., Sreenivasan, B., Mound, J., Rost, S., 2011. Melting of the Earth's inner core.
464 Nature 473, 361–U53.
465 Haigis, V., Salanne, M., Jahn, S., 2012. Thermal conductivity of MgO, MgSiO3 perovskite
466 and post-perovskite in the Earth's deep mantle. Earth Planet. Sci. Lett. 355-356,
467 102–108.
468 Hofmeister, A.M., 2008. Inference of high thermal transport in the lower mantle from laser-
469 flash experiments and the damped harmonic oscillator model. Phys. Earth Planet.
470 Inter. 170, 201–206.
471 Hofmeister, A.M., 2010. Thermal diffusivity of oxide perovskite compounds at elevated
472 temperature. J. Appl. Phys. 107, 103532.
473 Howell, P.C., 2011a. Thermal Conductivity Calculation with the Molecular Dynamics Direct
474 Method II: Improving the Computational Efficiency. J. Comput. Theor. Nanosci. 8,
475 2144–2154.
476 Howell, P.C., 2011b. Thermal Conductivity Calculation with the Molecular Dynamics Direct
477 Method I: More Robust Simulations of Solid Materials. J. Comput. Theor. Nanosci.
478 8, 2129–2143.

Howell, P.C., 2012. Comparison of molecular dynamics methods and interatomic potentials for calculating the thermal conductivity of silicon. J. Chem. Phys. 137, 224111.

Hu, L., Evans, W.J., Keblinski, P., 2011. One-dimensional phonon effects in direct molecular dynamics method for thermal conductivity determination. J. Appl. Phys. 110, 113511.

Imada, S., Ohta, K., Yagi, T., Hirose, K., Yoshida, H., Nagahara, H., 2014. Measurements of lattice thermal conductivity of MgO to core-mantle boundary pressures. Geophys. Rev. Lett. 41, 060423.

Keppler, H., Dubrovinsky, L.S., Narygina, O., Kantor, I., 2008. Optical Absorption and Radiative Thermal Conductivity of Silicate Perovskite to 125 Gigapascals. Science 322, 1529–1532.

Klemens, P., 1960. Thermal resistance due to point defects at high temperatures. Phys. Rev. 119, 507–509.

Kresse, G., Furthmuller, J., 1996a. Efficiency of ab-initio total energy calculations for metals and semiconductors using a plane-wave basis set. Comput. Mater. Sci. 6, 15–50.

Kresse, G., Furthmuller, J., 1996b. Efficient iterative schemes for ab initio total-energy calculations using a plane-wave basis set. Phys. Rev. B 54, 11169–11186.

Kustowski, B., Ekstrom, G., Dziewonski, A.M., 2008. Anisotropic shear-wave velocity structure of the Earth's mantle: A global model. J. Geophys. Res.-Solid Earth 113, B06306.

Lay, T., Hernlund, J., Buffett, B.A., 2008. Core-mantle boundary heat flow. Nat. Geosci. 1, 25–32.

Liao, B., Qiu, B., Zhou, J., Huberman, S., Esfarjani, K., Chen, G., 2015. Significant Reduction of Lattice Thermal Conductivity by the Electron-Phonon Interaction in

505 Silicon with High Carrier Concentrations: A First-Principles Study. Phys. Rev. Lett.
506 114, 115901.
507 Manga, M., Jeanloz, R., 1996. Implications of a metal-bearing chemical boundary layer in
508 D'' for mantle dynamics. Geophys. Res. Lett. 23, 3091–3094.
509 Manthilake, G.M., de Koker, N., Frost, D.J., McCammon, C.A., 2011. Lattice thermal
510 conductivity of lower mantle minerals and heat flux from Earth's core. Proc. Natl.
511 Acad. Sci. U. S. A. 108, 17901–17904.
512 Marquardt, H., Ganschow, S., Schilling, F.R., 2009a. Thermal diffusivity of natural and
513 synthetic garnet solid solution series. Phys. Chem. Miner. 36, 107–118.
514 Marquardt, H., Speziale, S., Reichmann, H.J., Frost, D.J., Schilling, F.R. 2009b. Single-
515 crystal elasticity of $(Mg_{0.9},Fe_{0.1})O$ to 81 GPa. Earth. Planet. Sci. Lett. 3-4, 345–352.
516 Muller-Plathe, F., 1997. A simple nonequilibrium molecular dynamics method for
517 calculating the thermal conductivity. J. Chem. Phys. 106, 6082–6085.
518 Nakagawa, T., Tackley, P.J., 2008. Lateral variations in CMB heat flux and deep mantle
519 seismic velocity caused by a thermal-chemical-phase boundary layer in 3D
520 spherical convection. Earth Planet. Sci. Lett. 271, 348–358.
521 Ni, S.D., Tan, E., Gurnis, M., Helmberger, D., 2002. Sharp sides to the African
522 superplume. Science 296, 1850–1852.
523 Nieto-Draghi, C., Avalos, J.B., 2003. Non-equilibrium momentum exchange algorithm for
524 molecular dynamics simulation of heat flow in multicomponent systems. Mol.
525 Phys. 101, 2303–2307.
526 Nose, S., 1984. A unified formulation of the constant temperature molecular dynamics
527 methods. J. Chem. Phys. 81, 511–519.
528 Ohta, K., Yagi, T., Hirose, K., 2014. Thermal diffusivities of MgSiO3 and Al-bearing
529 MgSiO3 perovskites. Am. Miner. 99, 94–97.

Ohta, K., Yagi, T., Taketoshi, N., Hirose, K., Komabayashi, T., Baba, T., Ohishi, Y., Hernlund, J., 2012. Lattice thermal conductivity of MgSiO3 perovskite and post-perovskite at the core-mantle boundary. Earth Planet. Sci. Lett. 349-350, 109–115.

Olson, P., Christensen, U.R., 2002. The time-averaged magnetic field in numerical dynamos with non-uniform boundary heat flow. Geophys. J. Int. 151, 809–823.

Osako, M., Ito, E., 1991. Thermal-diffusivity of MgSiO3 perovskite. Geophys. Res. Lett. 18, 239–242.

Perdew, J., Zunger, A., 1981. Self-interaction correction to density-functional approximations for many-electron systems. Phys. Rev. B 23, 5048–5079.

Rost, S., Garnero, E.J., Williams, Q., Manga, M., 2005. Seismological constraints on a possible plume root at the core-mantle boundary. Nature 435, 666–669.

Roufosse, M., Klemens, P., 1973. Thermal-conductivity of complex dielectric crystals. Phys. Rev. B 7, 5379–5386.

Roufosse, M., Klemens, P., 1974. Lattice thermal-conductivity of minerals at high-tempeatures. J. Geophys. Res. 79, 703–705.

Schelling, P.K., Phillpot, S.R., Keblinski, P., 2002. Comparison of atomic-level simulation methods for computing thermal conductivity. Phys. Rev. B 65.

Sellan, D.P., Landry, E.S., Turney, J.E., McGaughey, A.J.H., Amon, C.H., 2010. Size effects in molecular dynamics thermal conductivity predictions. Phys. Rev. B 81.

Stackhouse, S., Stixrude, L., 2010. Theoretical Methods for Calculating the Lattice Thermal Conductivity of Minerals, in: Wentzcovitch, R., Stixrude, L. (Eds.), Theoretical and Computational Methods in Mineral Physics: Geophysical Applications. Mineralogical Soc. Amer., Chantilly, pp. 253–269.

Stackhouse, S., Stixrude, L., Karki, B.B., 2010. Thermal Conductivity of Periclase (MgO) from First Principles. Phys. Rev. Lett. 104.

555 Stixrude, L., Lithgow-Bertelloni, C., 2011. Thermodynamics of mantle minerals - II. Phase
556 equilibria. Geophys. J. Int. 184, 1180–1213.
557 Tadano, T., Gohda, Y., Tsuneyuki, S., 2014. Anharmonic force constants extracted from
558 first-principles molecular dynamics: applications to heat transfer simulations. J.
559 Phys.-Condes. Matter 26, 225402.
560 Tang, X., Ntam, M.C., Dong, J., Rainey, E.S.G., Kavner, A., 2014. The thermal
561 conductivity of Earth's lower mantle. Geophysical Research Letters 41, 2746–2752.
562 Tsuchiya, T., Wentzcovitch, R.M., da Silva, C.R.S., de Gironcoli, S., 2006. Spin transition
563 in magnesiowustite in earth's lower mantle. Phys. Rev. Lett. 96.
564 Wentzcovitch, R.M., Justo, J.F., Wu, Z., da Silva, C.R.S., Yuen, D.A., Kohlstedt, D., 2009.
565 Anomalous compressibility of ferropericlase throughout the iron spin cross-over.
566 Proc. Natl. Acad. Sci. U. S. A. 106, 8447–8452.
567 Wookey, J., Stackhouse, S., Kendall, J.M., Brodholt, J., Price, G.D., 2005. Efficacy of the
568 post-perovskite phase as an explanation for lowermost-mantle seismic properties.
569 Nature 438, 1004–1007.
570 Zhou, X.W., Aubry, S., Jones, R.E., Greenstein, A., Schelling, P.K., 2009. Towards more
571 accurate molecular dynamics calculation of thermal conductivity: Case study of
572 GaN bulk crystals. Phys. Rev. B 79.
573

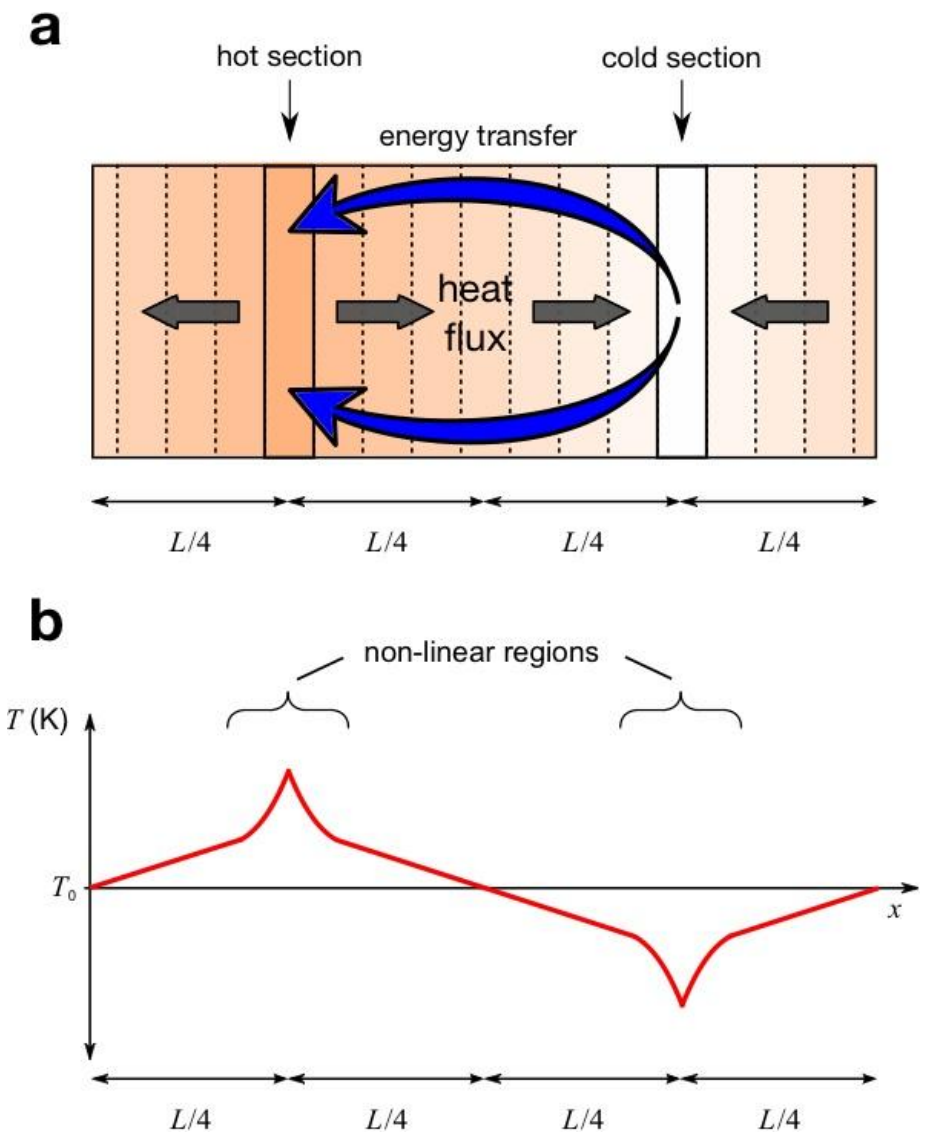

Fig. 1. The non-equilibrium molecular dynamics method for calculating lattice thermal conductivity. The simulation cell is split into sections of equal width. At regular intervals energy is transferred from the 'cold section' to the 'hot section', by means of a virtual elastic collision between the hottest atom in the cold section and coldest atom in the hot section. Due to the periodic nature of the simulation, two temperature gradients form. The non-Newtonian nature of the virtual elastic collision means that the temperature gradient is non-linear around the hot and cold sections. Figure after Stackhouse and Stixrude (2010).

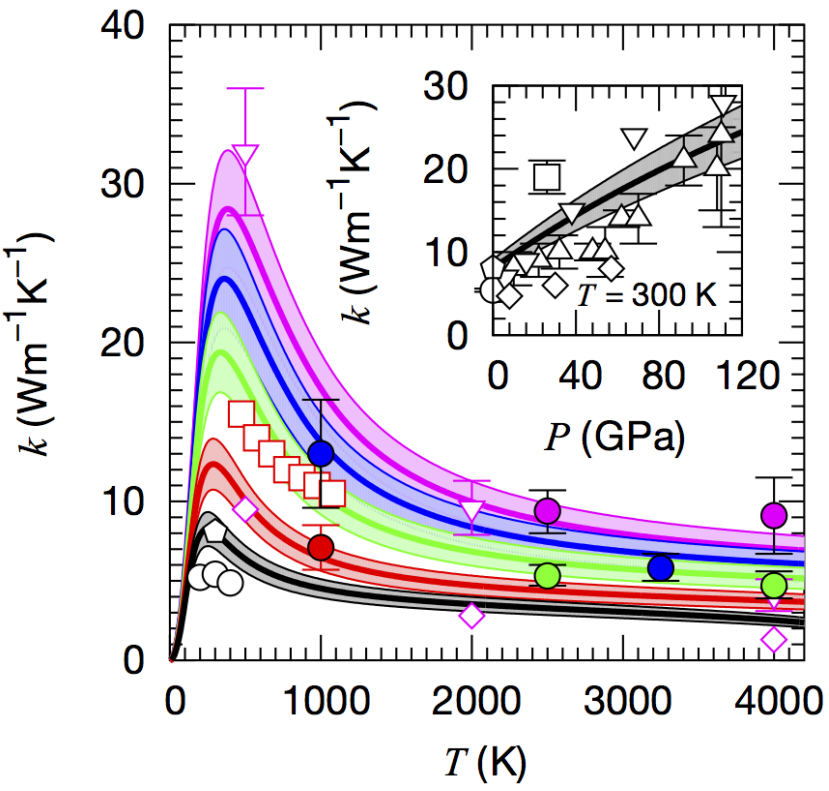

586

587 **Fig. 2**. Lattice thermal conductivity of $MgSiO_3$ perovskite as a function of temperature at
588 various pressures (main) and a function of pressure at 300 K (inset). Filled circles are the
589 results of our NEMD simulations and lines are the values predicted by our model
590 (described in the main text), with shading and error bars indicating standard error. Empty
591 symbols are measured (○ Osako and Ito (1991), □ Manthilake et al. (2011), △ Ohta et al.
592 (2012), □ Ohta et al. (2014)) and calculated (▽ Dekura et al. (2013), ◇ Tang et al. (2014))
593 values from previous studies. Color code for the main figure: black: 0 GPa, red:26 GPa,
594 green:75 GPa, blue:110 GPa and pink:145 GPa.

595

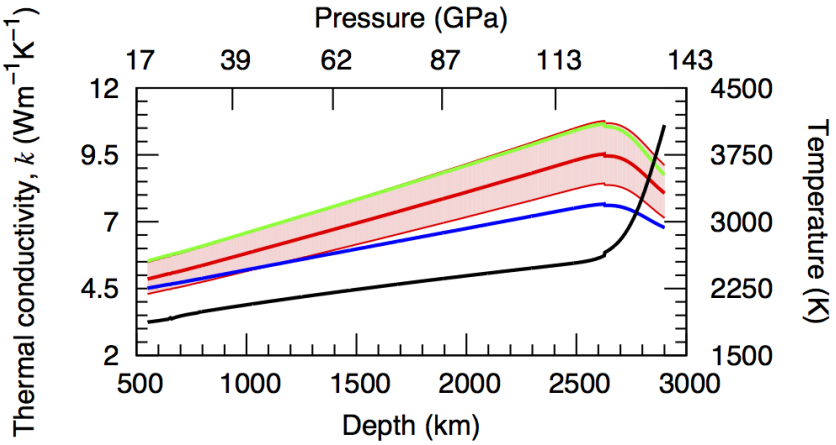

Fig. 3. Lattice thermal conductivity of a pyrolite mantle as a function of depth (red line, with the shading indicating standard error). Our results for pure $MgSiO_3$ perovskite (blue line) and iron-free pyrolite (green line) are shown for comparison. The geotherm (black line) is taken from a thermodynamic model (Stixrude and Lithgow-Bertelloni, 2011).

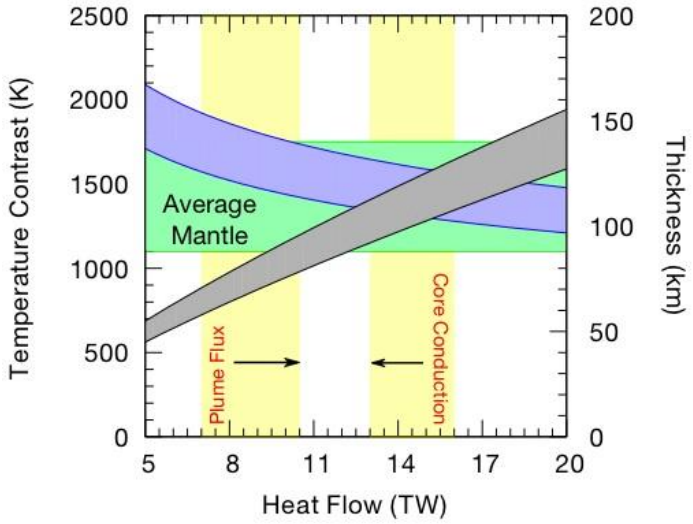

603

604 **Fig. 4.** Boundary layer analysis of heat flow. Temperature contrast ΔT (grey band) and
605 thickness δ (blue band) of the thermal boundary layer plotted against core-mantle
606 boundary heat flow, with the shading indicating the standard error in our determination of
607 the thermal conductivity (Supplementary Material Section S4). The green shaded area
608 denotes constraints on the temperature contrast across the core-mantle boundary. The
609 orange regions highlight constraints on the heat flow at the core-mantle boundary: upper
610 bound derived from the heat conducted down the core adiabat and lower bound derived
611 from the plume heat-flux and the factor 2-3 increase in the plume thermal anomaly with
612 depth (Davies, 2007).

613

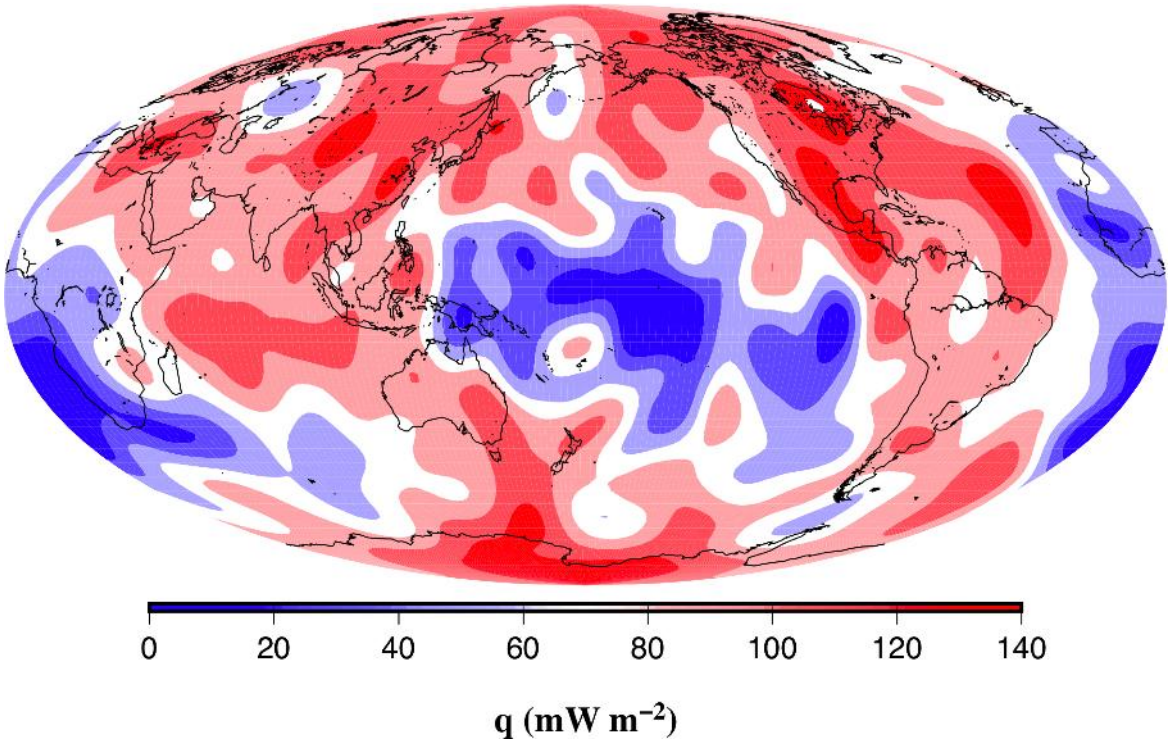

614
615

616 **Fig. 5.** Heat-flow at the core-mantle boundary. Values calculated from our estimate of

617 thermal conductivity and the seismic tomographic model of Kustowski et al. (2008) at 2800

618 km depth.

619